

Nonlinear Dendritic Coincidence Detection for Supervised Learning

Fabian Schubert^{1,*} and Claudius Gros¹

¹ Institute for Theoretical Physics, Goethe University Frankfurt am Main, Germany

Correspondence*:

Institute for Theoretical Physics
Goethe University Frankfurt am Main
Max-von-Laue-Str. 1
60438 Frankfurt am Main, Germany
fschubert@itp.uni-frankfurt.de

2 ABSTRACT

3 Cortical pyramidal neurons have a complex dendritic anatomy, whose function is an active
4 research field. In particular, the segregation between its soma and the apical dendritic tree is
5 believed to play an active role in processing feed-forward sensory information and top-down
6 or feedback signals. In this work, we use a simple two-compartment model accounting for
7 the nonlinear interactions between basal and apical input streams and show that standard
8 unsupervised Hebbian learning rules in the basal compartment allow the neuron to align the
9 feed-forward basal input with the top-down target signal received by the apical compartment.
10 We show that this learning process, termed coincidence detection, is robust against strong
11 distractions in the basal input space and demonstrate its effectiveness in a linear classification
12 task.

13 **Keywords:** Dendrites, Pyramidal Neuron, Plasticity, Coincidence Detection, Supervised Learning

1 INTRODUCTION

14 In recent years, a growing body of research has addressed the functional implications of the distinct
15 physiology and anatomy of cortical pyramidal neurons (Spruston, 2008; Hay et al., 2011; Ramaswamy and
16 Markram, 2015). In particular, on the theoretical side, we saw a paradigm shift from treating neurons as
17 point-like electrical structures towards embracing the entire dendritic structure (Larkum et al., 2009; Poirazi,
18 2009; Shai et al., 2015). This was mostly due to the fact that experimental work uncovered dynamical
19 properties of pyramidal neuronal cells that simply could not be accounted for by point models (Spruston
20 et al., 1995; Häusser et al., 2000).

21 An important finding is that the apical dendritic tree of cortical pyramidal neurons can act as a separate
22 nonlinear synaptic integration zone (Spruston, 2008; Branco and Häusser, 2011). Under certain conditions,
23 a dendritic Ca^{2+} spike can be elicited that propagates towards the soma, causing rapid, bursting spiking
24 activity. One of the cases in which dendritic spiking can occur was termed ‘backpropagation-activated Ca^{2+}
25 spike firing’ (‘BAC firing’): A single somatic spike can backpropagate towards the apical spike initiation
26 zone, in turn significantly facilitating the initiation of a dendritic spike (Stuart and Häusser, 2001; Spruston,
27 2008; Larkum, 2013). This reciprocal coupling is believed to act as a form of coincidence detection: If
28 apical and basal synaptic input co-occurs, the neuron can respond with a rapid burst of spiking activity.
29 The firing rate of these temporal bursts exceeds the firing rate that is maximally achievable under basal

30 synaptic input alone, therefore representing a form of temporal coincidence detection between apical and
31 basal input.

32 Naturally, these mechanisms also affect plasticity, and thus learning within the cortex (Sjöström and
33 Häusser, 2006; Ebner et al., 2019). While the interplay between basal and apical stimulation and its effect
34 on synaptic efficacies is subject to ongoing research, there is evidence that BAC-firing tends to shift
35 plasticity towards long-term potentiation (LTP) (Letzkus et al., 2006). Thus, coincidence between basal
36 and apical input appears to also gate synaptic plasticity.

37 In a supervised learning scheme, where the top-down input arriving at the apical compartment acts as the
38 teaching signal, the most straight-forward learning rule for the basal synaptic weights would be derived
39 from an appropriate loss function, such as a mean square error, based on the difference between basal and
40 apical input, i.e. $I_p - I_d$, where indices p and d denote ‘proximal’ and ‘distal’, in equivalence to basal and
41 apical. Theoretical studies have investigated possible learning mechanisms that could utilize an intracellular
42 error signal (Urbanczik and Senn, 2014; Schiess et al., 2016; Guergiev et al., 2017). However, a clear
43 experimental evidence for a physical quantity encoding such an error is—to our knowledge—yet to be
44 found. On the other hand, Hebbian-type plasticity is extensively documented in experiments (Gustafsson
45 et al., 1987; Debanne et al., 1994; Markram et al., 1997; Bi and Poo, 1998). Therefore, our work is based
46 on the question of whether the nonlinear interactions between basal and apical synaptic input could, when
47 combined with a Hebbian plasticity rule, allow a neuron to learn to reproduce an apical teaching signal in
48 its proximal input.

49 We investigate coincidence learning by combining a phenomenological model that generates the output
50 firing rate as a function of two streams of synaptic input (subsuming basal and apical inputs) with classical
51 Hebbian, as well as BCM-like plasticity rules on basal synapses. In particular, we hypothesized that this
52 combination of neural activation and plasticity rules would lead to an increased correlation between basal
53 and apical inputs. Furthermore, the temporal alignment observed in our study could potentially facilitate
54 apical inputs to act as top-down teaching signals, without the need for an explicit error-driven learning
55 rule. Thus, we also test our model in a simple linear supervised classification task and compare it with the
56 performance of a simple point neuron equipped with similar plasticity rules.

2 MODEL

57 2.1 Compartmental Neuron

The neuron model used throughout this study is a discrete-time rate encoding model that contains two separate input variables, representing the total synaptic input current injected arriving at the basal (proximal) and apical (distal) dendritic structure of a pyramidal neuron, respectively. The model is a slightly simplified version of a phenomenological model proposed by Shai et al. (2015). Denoting the input currents I_p (proximal) and I_d (distal), the model is written as

$$y(t) = \alpha \sigma(I_p(t) - \theta_{p0}) [1 - \sigma(I_d(t) - \theta_d)] + \sigma(I_d(t) - \theta_d) \sigma(I_p(t) - \theta_{p1}) \quad (1)$$

$$\sigma(x) \equiv \frac{1}{1 + \exp(-4x)}. \quad (2)$$

58 Here, $\theta_{p0} > \theta_{p1}$ and θ_d are threshold variables with respect to proximal and distal inputs. Equation (1)
59 defines the firing rate y as a function of I_p and I_d . Note that the firing rate is normalized to take values
60 within $y \in [0, 1]$. In the publication by Shai et al. (2015), firing rates varied between 0 and 150 Hz. High

61 firing rates typically appear in the form of bursts of action potentials, lasting on the order of 50–100 ms
 62 Larkum et al. (1999); Shai et al. (2015). Therefore, since our model represents “instantaneous” firing rate
 63 responses to a discrete set of static input patterns, we conservatively estimate the time scale of our model
 64 to be on the order of tenths of seconds.

65 In general, the input currents I_p and I_d are meant to comprise both excitatory and potential inhibitory
 66 currents. Therefore, we did not restrict the sign of of I_p and I_d to positive values. Moreover, since we chose
 67 the thresholds θ_{p0} and θ_d to be zero, I_p and I_d should be rather seen as a total external input relative to
 68 intrinsic firing thresholds.

69 Note that the original form of this phenomenological model by Shai et al. (2015) is of the form

$$y(I_p, I_d) = \sigma(I_p - A\sigma(I_d)) [1 + B\sigma(I_d)] , \quad (3)$$

70 where σ denotes the same sigmoidal activation function. This equation illustrates that I_d has two effects:
 71 It shifts the basal activation threshold by a certain amount (here controlled by the parameter A) and also
 72 multiplicatively increases the maximal firing rate (to an extent controlled by B). Our equation mimics these
 73 effects by means of the two thresholds θ_{p0} and θ_{p1} , as well as the value of α relative to the maximal value
 74 of y (which is 1 in our case).

75 Overall, equation (1) describes two distinct regions of neural activation in the (I_p, I_d) -space which differ
 76 in their maximal firing rates, which are set to 1 and α , where $0 < \alpha < 1$. A plot of (1) is shown in Fig. 1.

77 When both input currents I_d and I_p are large, that is, larger than the thresholds θ_d and θ_{p1} , the second
 78 term in (1) dominates, which leads to $y \approx 1$. An intermediate activity plateau, of strength α emerges in
 79 addition when $I_p > \theta_{p0}$ and $I_d < \theta_d$. As such, the compartment model (1) is able to distinguish neurons
 80 with a normal activity level, here encoded by $\alpha = 0.3$, and strongly bursting neurons, where the maximal
 81 firing rate is unity. The intermediate plateau allows neurons to process the proximal inputs I_p even in the
 82 absence of distal stimulation. The distal current I_d acts therefore as an additional modulator.

83 In our numerical experiments, we compare the compartment model with a classical point neuron, as
 84 given by

$$y(t) = \sigma(I_p(t) + I_d(t) - \theta) . \quad (4)$$

85 The apical input I_d is generated ‘as is’, meaning it is not dynamically calculated as a superposition of
 86 multiple presynaptic inputs. For concreteness, we used

$$I_d(t) = n_d(t)x_d(t) - b_d(t) , \quad (5)$$

87 where $n_d(t)$ is a scaling factor, $x_d(t)$ a discrete time sequence, which represents the target signal to be
 88 predicted by the proximal input, and $b_d(t)$ a bias. In our experiments, we chose x_d according to the
 89 prediction task at hand, see (17) and (19)–(20).

90 Note that n_d and b_d are time dependent since they are subject to adaptation processes, which will be
 91 described in the next section. Similarly, the proximal input $I_p(t)$ is given by

$$I_p(t) = n_p(t) \sum_{i=1}^N x_{p,i}(t)w_i(t) - b_p(t) , \quad (6)$$

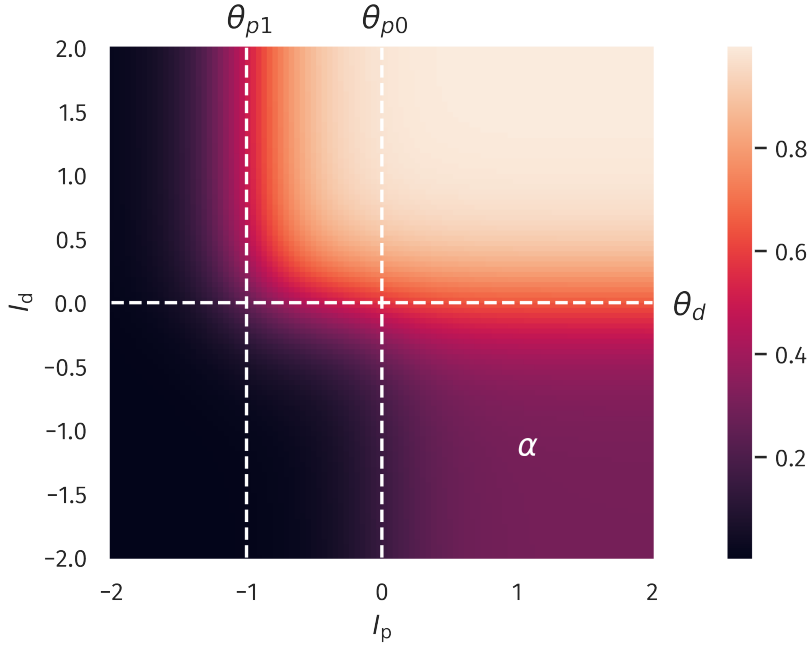


Figure 1. Two-compartment rate model. The firing rate as a function of proximal and distal inputs I_p and I_d , see (1). The thresholds θ_{p0} , θ_{p1} and θ_d define two regions of neural activity, with a maximal firing rate of 1 and a plateau in the lower-left quadrant with a value of $\alpha = 0.3$. That is, the latter region can achieve 30% of the maximal firing rate.

92 where N is the number of presynaptic afferents, $x_{p,i}(t)$ the corresponding sequences, $w_i(t)$ the synaptic
 93 efficacies and $n_p(t)$ and $b_p(t)$ the (time dependent) scaling and bias. Tyical values for the parameters used
 94 throughout this study are presented in Table 1.

95 2.2 Homeostatic Parameter Regulation

The bias variables entering the definitions (5) and (6) of the distal proximal current, I_d and I_p , are assumed to adapt according to

$$b_p(t+1) = b_p(t) + \mu_b [I_p(t) - I_p^t] \quad (7)$$

$$b_d(t+1) = b_d(t) + \mu_b [I_d(t) - I_d^t], \quad (8)$$

96 where $I_p^t = 0$ and, $I_d^t = 0$ are preset targets and $1/\mu_b = 10^3$ is the timescale for the adaption. Since this is
 97 a slow process, over time, both the distal and the proximal currents, I_d and I_p , will approach a temporal
 98 mean equal to I_p^t and I_d^t respectively while still allowing the input to fluctuate. The reason for choosing
 99 the targets to be zero lies in the fact that we expect a neuron to operate in a dynamical regime that can
 100 reliably encode information from its inputs. In the case of our model, this implies that neural input should
 101 be distributed close to the threshold (which was set to zero in our case), such that fluctuations in the can
 102 have an effect on the resulting neural activity. See e.g. Bell and Sejnowski (1995) and Triesch (2007) for
 103 theoretical approaches to optimizing gains and biases based on input and output statistics. Hence, while we
 104 chose the mean targets of the input to be the same as the thresholds, this is not a strict condition, as relevant
 105 information in the input could also be present in parts of the input statistics that significantly differ from its
 106 actual mean (for example in the case of a heavily skewed distribution).

Adaptation rules for the bias entering a transfer function, such as (8) and (7), have the task to regulate overall activity levels. The overall magnitude of the synaptic weights, which are determined by synaptic rescaling factors, here n_d and n_p , as defined in (5) and (6), will regulate in contrast the variance of the neural activity, and not the average level (Schubert and Gros, 2021). In this spirit we consider

$$n_d(t+1) = n_d(t) + \mu_n \left[V_d^t - \left(I_d(t) - \tilde{I}_d(t) \right)^2 \right] \quad (9)$$

$$n_p(t+1) = n_p(t) + \mu_n \left[V_p^t - \left(I_p(t) - \tilde{I}_p(t) \right)^2 \right] \quad (10)$$

$$\tilde{I}_d(t+1) = (1 - \mu_{\text{av}}) \tilde{I}_d(t) + \mu_{\text{av}} I_d(t) \quad (11)$$

$$\tilde{I}_p(t+1) = (1 - \mu_{\text{av}}) \tilde{I}_p(t) + \mu_{\text{av}} I_p(t) . \quad (12)$$

107 Here, V_p^t and V_d^t define targets for the temporally averaged variances of I_p and I_d . The dynamic variables
 108 \tilde{I}_p and \tilde{I}_d are simply low-pass filtered running averages of I_p and I_d . Overall, the framework specified here
 109 allows the neuron to be fully flexible, as long as the activity level and its variance fluctuate around preset
 110 target values (Schubert and Gros, 2021).

111 Mapping the control of the mean input current to the biases and the control of variance to the gains is,
 112 in a sense, an idealized case of the more general notion of dual homeostasis. As shown by Cannon and
 113 Miller (2017), the conditions for a successful control of mean and variance by means of gains and biases
 114 are relatively loose: Under certain stability conditions, a combination of two nonlinear functions of the
 115 variable that is to be controlled can yield a dynamic fixed point associated with a certain mean and variance.
 116 In fact, a possible variant of dual homeostasis could potentially be achieved by coupling the input gains to
 117 a certain firing rate (which is a non-linear function of the input), while biases are still adjusted to a certain
 118 mean input. This, of course, would make it harder to predict the variance of the input resulting from such
 119 an adaptation, since it would not enter the equations as a simple parameter that can be chosen a priori (as it
 120 is the case for equation (11) and (12)).

121 A list of the parameter values used throughout this investigation is also given in Table 1. Our choices
 122 of target means and variances are based on the assumption that neural input should be tuned towards a
 123 certain working regime of the neural transfer function. In the case of the presented model, this means that
 124 both proximal and distal input cover an area where the nonlinearities of the transfer function are reflected
 125 without oversaturation.

Table 1. Model parameters, as defined in sections 2.1 and 2.3.

θ_{p0}	0	V_d^t	0.25
θ_{p1}	-1	μ_b	10^{-3}
θ_d	0	μ_n	10^{-4}
α	0.3	μ_{av}	$5 \cdot 10^{-3}$
μ_w	$5 \cdot 10^{-5}$	I_p^t	0
ϵ	0.1	I_d^t	0
V_p^t	0.25		

126 **2.3 Synaptic Plasticity**

The standard Hebbian plasticity rule for the proximal synaptic weights is given by

$$w_i(t+1) = w_i(t) + \mu_w [(x_{p,i}(t) - \tilde{x}_{p,i}(t)) (y(t) - \tilde{y}) - \epsilon w_i(t)] \quad (13)$$

$$\tilde{x}_{p,i}(t+1) = (1 - \mu_{av})\tilde{x}_{p,i}(t) + \mu_{av}x_{p,i}(t) \quad (14)$$

$$\tilde{y}(t+1) = (1 - \mu_{av})\tilde{y}(t) + \mu_{av}y(t) \quad (15)$$

127 The trailing time averages $\tilde{x}_{p,i}$ and \tilde{y} , respectively of the presynaptic basal activities, $x_{p,i}$, and of the neural
 128 firing rate y , enter the Hebbian learning rule (13) as reference levels. Pre- and post-synaptic neurons
 129 are considered to be active/inactive when being above/below the respective trailing averages. This is a
 130 realization of the Hebbian rule proposed by Linsker (1986). The timescale of the averaging, $1/\mu_{av}$, is 200
 131 time steps, see Table 1. As discussed in Section 2.1, a time step can be considered to be on the order of
 132 100 ms, which equates to an averaging time of about 20 s. Generally, this is much faster than the timescales
 133 on which metaplasticity, i.e. adaptation processes affecting the dynamics of synaptic plasticity itself, are
 134 believed to take place, which are on the order of days (Yger and Gilson, 2015). However, it should be noted
 135 that our choice of the timescale of the averaging process used in our plasticity model is motivated mostly
 136 by considerations regarding the overall simulation time: Given enough update steps, the same results could
 137 be achieved by an arbitrarily slow averaging process.

138 Since classical Hebbian learning does not keep weights bounded, we use an additional proportional decay
 139 term ϵw_i which prevents runaway growth using $\epsilon = 0.1$. With $1/\mu_w = 2 \cdot 10^4$, learning is assumed to be
 140 considerably slower, as usual for statistical update rules. For comparative reasons, the point neuron model
 141 (4) is equipped with the same plasticity rule for the proximal weights as (13).

142 Apart from classical Hebbian learning, we also considered a BCM-like learning rule for the basal weights
 143 (Bienenstock et al., 1982; Intrator and Cooper, 1992). The form of the BCM-rule used here reads

$$w_i(t+1) = w_i(t) + \mu_w [y(y - \theta_M)x_i - \epsilon w_i], \quad (16)$$

144 where θ_M is a threshold defining a transition from long-term potentiation (LTP) to long-term depression
 145 (LTD) and, again, ϵ is a decay term on the weights preventing unbounded growth. In the variant introduced
 146 by Law and Cooper (1994), the sliding threshold is simply the temporal average of the squared neural
 147 activity, $\theta_M = \langle y^2 \rangle$. In practice, this would be calculated as a running average, thereby preventing the
 148 weights from growing indefinitely.

149 However, for our compartment model, we chose to explicitly set the threshold to be the mean value
 150 between the high- and low-activity regime in our compartment model, i.e. $\theta_M = (1 + \alpha)/2$. By doing so,
 151 LTP is preferably induced if both basal and apical input is present at the same time. Obviously, for the point
 152 model, the reasoning behind our choice of θ_M did not apply. Still, to provide some level of comparability,
 153 we also ran simulations with a point model where the sliding threshold was calculated as a running average
 154 of y^2 .

3 RESULTS

155 **3.1 Unsupervised Alignment between Basal and Apical Inputs**

156 As a first test, we quantify the neuron's ability to align its basal input to the apical teaching signal. This can
 157 be done using the Pearson correlation coefficient $\rho[I_p, I_d]$ between the basal and apical input currents. We

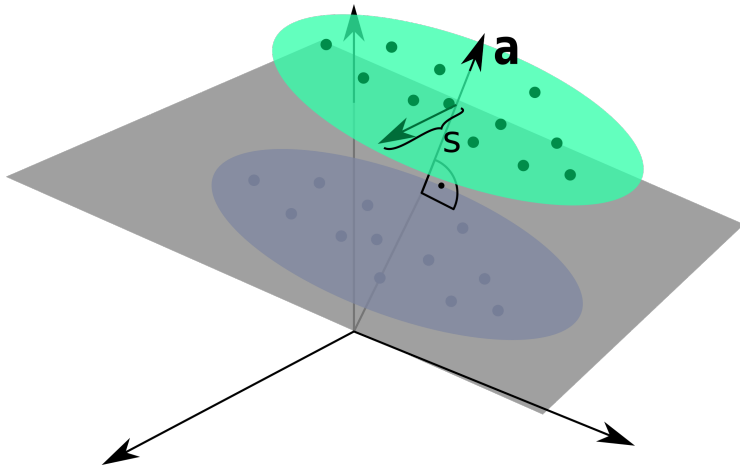


Figure 2. Input Space for the Linear Classification Task. Two clusters of presynaptic basal activities were generated from multivariate Gaussian distributions. Here, s denotes the standard deviation orthogonal to the normal vector a of the classification hyperplane, as defined by (17).

158 determined $\rho[I_p, I_d]$ after the simulation, which involves all plasticity mechanisms, both for the synaptic
 159 weights and the intrinsic parameters. The input sequences $x_{p,i}(t)$ is randomly drawn from a uniform
 160 distribution, in $[0, 1]$, which is done independently for each $i \in [1, N]$.

For the distal current $I_d(t)$ to be fully ‘reconstructable’ by the basal input, $x_d(t)$ has to be a linear combination

$$x_d(t) = \sum_{i=1}^N a_i x_{p,i}(t) \quad (17)$$

161 of the $x_{p,i}(t)$, where the a_i are the components of a random vector a of unit length.

162 Given that we use with (13) a Hebbian learning scheme, one can expect that the direction and the
 163 magnitude of the principal components of the basal input may affect the outcome of the simulation
 164 significantly: A large variance in the basal input orthogonal to the ‘reconstruction vector’ a is a distraction
 165 for the plasticity. The observed temporal alignment between I_p and I_d should hence suffer when such a
 166 distraction is present.

167 In order to test the effects of distracting directions, we applied a transformation to the input sequences
 168 $x_{p,i}(t)$. For the transformation, two parameters are used, a scaling factor s and the dimension N_{dist} of the
 169 distracting subspace within the basal input space. The N_{dist} randomly generated basis vectors are orthogonal
 170 to the superposition vector a , as defined by (17), and to each others. Within this N_{dist} -dimensional subspace,
 171 the input sequences $x_{p,i}(t)$ are rescaled subsequently by the factor s . After the learning phase, a second set
 172 of input sequences $x_{p,i}(t)$ and $x_d(t)$ is generated for testing purposes, using the identical protocol, and the
 173 cross correlation $\rho[I_p, I_d]$ evaluated. During the testing phase plasticity is turned off.

174 The overall aim of our protocol is to evaluate the degree $\rho[I_p, I_d]$ to which the proximal current I_p aligns
 175 in the temporal domain to the distal input I_d . We recall that this is a highly non-trivial question, given that
 176 the proximal synaptic weights are adapted via Hebbian plasticity, see (13). The error $(I_p - I_d)^2$ does not
 177 enter the adaption rules employed. Results are presented in Fig. 3 as a function of the distraction parameters
 178 s and $N_{\text{dist}} \in [0, N - 1]$. The total number of basal inputs is $N = 100$.

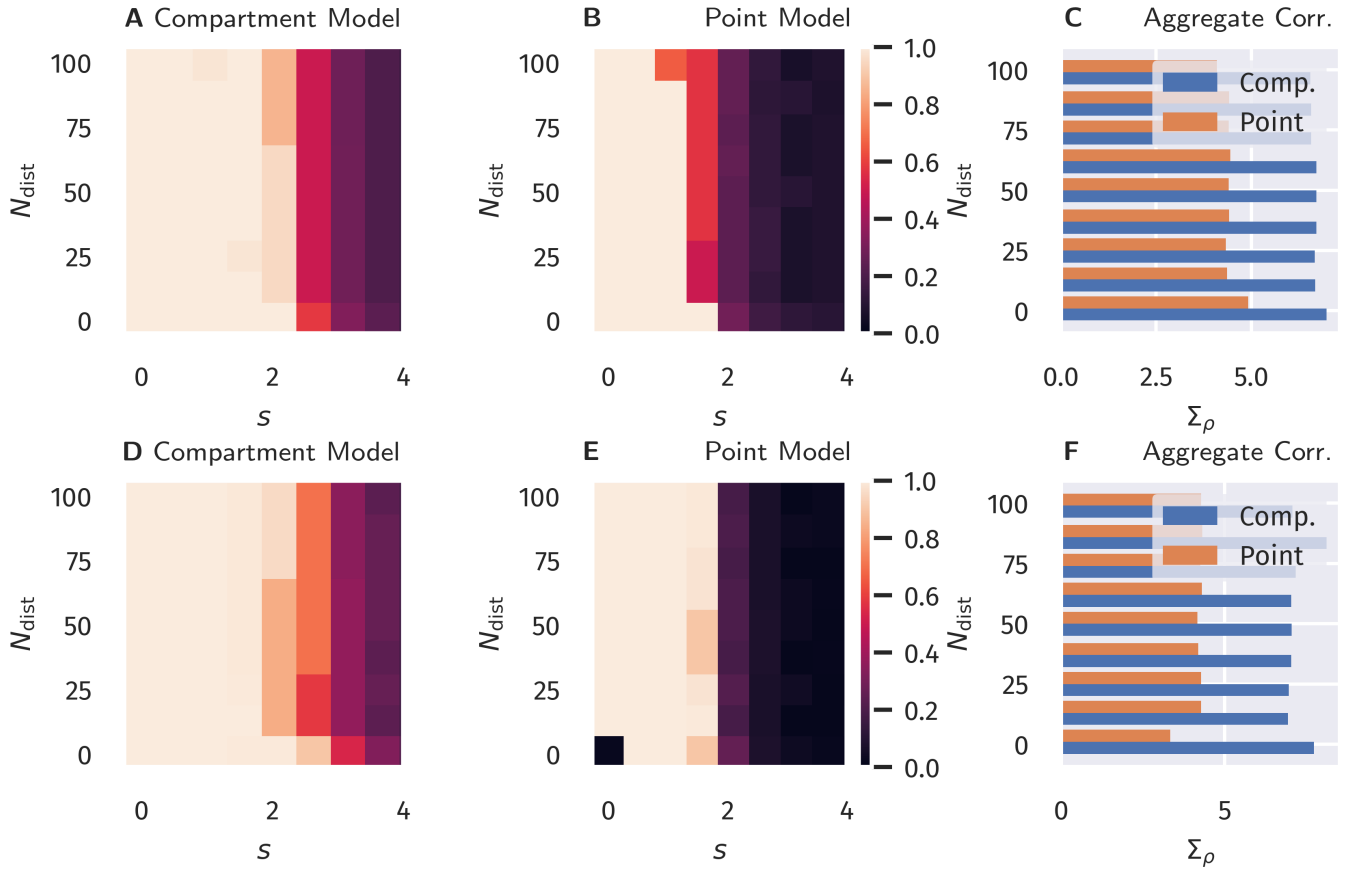


Figure 3. Unsupervised Alignment between Basal and Apical Input. Color encoded is the Pearson correlation $\rho[I_p, I_d]$ between the proximal and distal input currents, I_p and I_d . A–C: Classical Hebbian plasticity, as defined by (13). D–F: BCM rule, see (16). Data for a range $N_{\text{dist}} \in [0, N - 1]$ of the orthogonal distraction directions, and scaling factors s , as defined in Fig. 2. The overall number of basal inputs is $N = 100$. In the bar plot on the right the sum Σ_{acc} over $s = 0, 0.5, 1.0 \dots$ of the results is shown as a function of N_{dist} . Blue bars represents the compartment model, orange the point model.

179 For comparison, in Fig. 3 data for both the compartment model and for a point neuron are presented (as
 180 defined respectively by (1) and (4)), as well as results for both classical Hebbian and BCM learning rules.
 181 A decorrelation transition as a function of the distraction scaling parameter s is observed for both models
 182 and plasticity rules. In terms of the learning rules, only marginal differences are present. However, the
 183 compartment model is able to handle a significantly stronger distraction as compared to the point model.
 184 These findings support the hypothesis examined here, namely that nonlinear interactions between basal and
 185 apical input improve learning guided by top-down signals.

186 3.2 Supervised Learning in a Linear Classification Task

187 Next, we investigated if the observed differences would also improve the performance in an actual
 188 supervised learning task. For this purpose, we constructed presynaptic basal input $x_p(t)$ as illustrated in
 189 Fig. 2. Written in vector form, each sample from the basal input is generated from,

$$\mathbf{x}_p(t) = \mathbf{b} + \mathbf{a}[c(t) + \sigma_a \zeta_a(t)] + s \cdot \sum_{i=1}^{N_{\text{dist}}} \zeta_{\text{dist},i}(t) \mathbf{v}_{\text{dist},i}, \quad (18)$$

190 where \mathbf{b} is a random vector, where each entry is drawn uniformly from $[0, 1]$, \mathbf{a} is random unit vector as
 191 introduced in Section 3.1, $c(t)$ is a binary variable drawn from $\{-0.5, 0.5\}$ with equal probability and $\zeta_a(t)$
 192 and the $\zeta_{dist,i}(t)$ are independent Gaussian random variables with zero mean and unit variance. Hence, σ_a
 193 simply denotes the standard deviation of each Gaussian cluster along the direction of the normal vector \mathbf{a}
 194 and was set to $\sigma_a = 0.25$. Finally, the set of $\mathbf{v}_{dist,i}$ forms a randomly generated orthogonal basis of N_{dist}
 195 unit vectors which are—as in Section 3.1—also orthogonal to \mathbf{a} . The free parameter s parameterizes the
 196 standard deviation along this subspace orthogonal to \mathbf{a} . As indicated by the time dependence, the Gaussian
 197 and binary random variables are drawn for each time step. The vectors \mathbf{b} , \mathbf{a} , and $\mathbf{v}_{dist,i}$ are generated once
 198 before the beginning of a simulation run.

For the classification task, we use two output neurons, indexed 0 and 1, receiving the same basal presynaptic input, with the respective top-down inputs $x_{d,0}$ and $x_{d,1}$ encoding the desired linear classification in a one-hot scheme,

$$x_{d,0}(t) = 1 - \Theta \left((\mathbf{x}_p(t) - \mathbf{b})^T \mathbf{a} \right) \quad (19)$$

$$x_{d,1}(t) = \Theta \left((\mathbf{x}_p(t) - \mathbf{b})^T \mathbf{a} \right), \quad (20)$$

199 where $\Theta(x)$ is the Heaviside step function.

200 As in the previous experiment, we ran a full simulation until all dynamic variables reached a stationary
 201 state. After this, a test run without plasticity and with the apical input turned off was used to evaluate the
 202 classification performance. For each sample, the index of the neuron with the highest activity was used as
 203 the predicted class. Accuracy was then calculated as the fraction of correctly classified samples.

204 The resulting accuracy as a function of N_{dist} and s is shown in Fig. 4, again for all four combinations of
 205 neuron models and learning rules.

206 For classical Hebbian plasticity, the differences between compartmental and point neuron are small.
 207 Interestingly, the compartment model performs measurably better in the case of the BCM rule (16), in
 208 particular when the overall accuracies for the tested parameter range are compared, see Fig. 4D. This
 209 indicates that during learning, the compartmental neuron makes better use, of the three distinct activity
 210 plateaus at 0, α and 1, when the BCM rule is at work. Compare Fig. 1. We point out in this respect that the
 211 sliding threshold θ_M in (16) has been set to the point halfway between the two non-trivial activity levels, α
 212 and 1.

213 It should be noted that the advantage of the compartment model is also reflected in the actual correlation
 214 between proximal and distal input as a measure of successful learning (as done in the previous section), see
 215 Fig. 5 in the appendix. Interestingly, the discrepancies are more pronounced when measuring the correlation
 216 as compared to the accuracy. Moreover, it appears that above-chance accuracy is still present for parameter
 217 values where alignment is almost zero. We attribute this effect to the fact that the classification procedure
 218 predicts the class by choosing the node that has the higher activity, independent of the actual “confidence”
 219 of this prediction, i.e. how strong activities differ relative to their actual activity levels. Therefore, marginal
 220 differences can still yield the correct classification in this isolated setup, but it would be easily disrupted by
 221 finite levels of noise or additional external input.

4 DISCUSSION

222 Pyramidal neurons in the brain possess distinct apical/basal (distant/proximal) dendritic trees. It is hence
 223 likely that models with at least two compartments are necessary for describing the functionality of

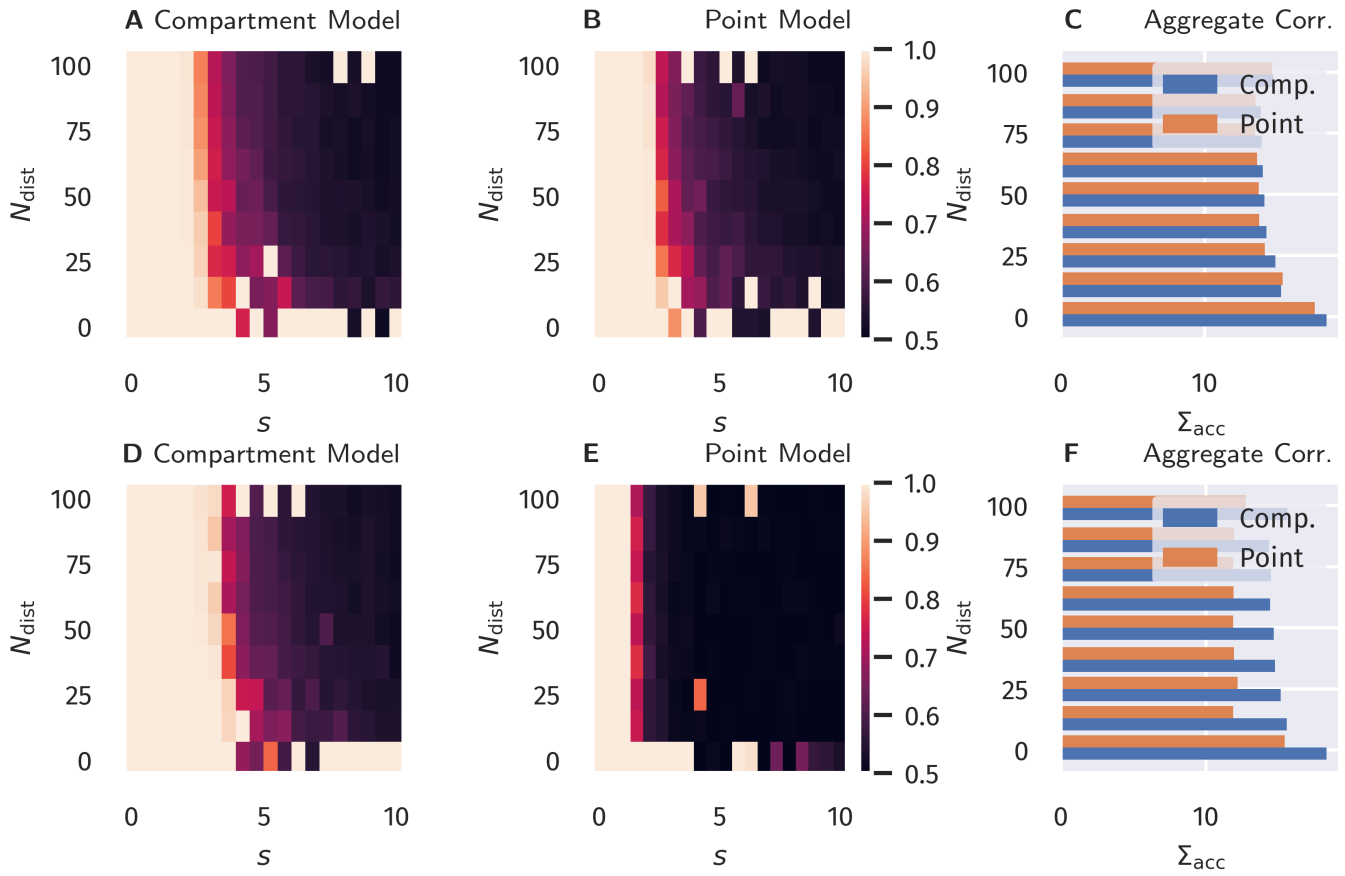


Figure 4. Binary Classification Accuracy. Fraction of correctly classified patterns as illustrated in Fig. 2, see Section 3.2. A–C: Classical Hebbian plasticity. D–F: BCM rule. In the bar plot on the right the sum Σ_{acc} over $s = 0, 0.5, 1.0..$ of the results is given as a function of N_{dist} . Blue bars represents the compartment model, orange the point model.

224 pyramidal neurons. For a proposed two-compartment transfer function (Shai et al., 2015), we have
 225 introduced both unsupervised and supervised learning schemes, showing that the two-compartment neuron
 226 is significantly more robust against distracting components in the proximal input space than a corresponding
 227 (one-compartment) point neuron.

228 The apical and basal dendritic compartments of pyramidal neurons are located in different cortical layers
 229 Park et al. (2019), receiving top-down and feed-forward signals, respectively. The combined action of these
 230 two compartments is hence the prime candidate for the realization of backpropagation in multi-layered
 231 networks (Bengio, 2014; Lee et al., 2015; Guergiev et al., 2017).

232 4.1 Learning Targets by Maximizing Correlation

233 In the past, backpropagation algorithms for pyramidal neurons concentrated on learning rules that are
 234 explicitly dependent on an error term, typically the difference between top-down and bottom-up signals.
 235 In this work, we considered an alternative approach. We postulate that the correlation between proximal
 236 and distal input constitutes a viable objective function, which is to be maximized in combination with
 237 homeostatic adaptation rules that keep proximal and distal inputs within desired working regimes. Learning
 238 correlations between distinct synaptic or compartmental inputs is as a standard task for Hebbian-type
 239 learning, which implies that the here proposed framework is based not on supervised, but on biologically
 240 viable unsupervised learning schemes.

241 The proximal input current I_p is a linear projection of the proximal input space. Maximizing the
242 correlation between I_p and I_d (the distal current), can therefore be regarded as a form of canonical
243 correlation analysis (CCA) (Härdle and Simar, 2007). The idea of using CCA as a possible mode of
244 synaptic learning has previously been investigated by Haga and Fukai (2018). Interestingly, according to
245 the authors, a BCM-learning term in the plasticity dynamics accounts for a principal component analysis
246 in the input space, while CCA requires an additional multiplicative term between local basal and apical
247 activity. In contrast, our results indicate that such a multiplicative term is not required to drive basal
248 synaptic plasticity towards a maximal alignment between basal and apical input, even in the presence
249 of distracting principal components. Apart from the advantage that this avoids the necessity of giving a
250 biophysical interpretation of such cross-terms, it is also in line with the view that synaptic plasticity should
251 be formulated in terms of local membrane voltage traces (Clopath et al., 2010; Weissenberger et al., 2018).
252 According to this principle, distal compartments should therefore only implicitly affect plasticity in basal
253 synapses, e.g. by facilitating spike initiation.

254 4.2 Generalizability of the Model to Neuroanatomical Variability

255 While some research on cortical circuits suggests the possibility of generic and scalable principles that apply
256 to different cortical regions and their functionality (Douglas and Martin, 2007; George and Hawkins, 2009;
257 Larkum, 2013), it is also well known that the anatomical properties of pyramidal neurons, in particular
258 the dendritic structure, varies significantly across cortical regions (Fuster, 1973; Funahashi et al., 1989).
259 More specifically, going from lower to higher areas of the visual pathway, one can observe a significant
260 increase of spines in the basal dendritic tree (Elston and Rosa, 1997; Elston, 2000), which can be associated
261 with the fact that neurons in higher cortical areas generally encode more complex or even multi-sensory
262 information, requiring the integration of activity from a higher number and potentially more distal neurons
263 (Elston, 2003; Luebke, 2017).

264 With respect to a varying amount of basal synaptic inputs, it is interesting to note that the dimensionality
265 N of the basal input patterns did not have a large effect on the results of our model, see Fig. 3–5, as long as
266 the homeostatic processes provided weight normalization.

267 Apart from variations in the number of spines, variability can also be observed within the dendritic
268 structure itself (Spruston, 2008; Ramaswamy and Markram, 2015). Such differences obviously affect
269 the internal dynamics of the integration of synaptic inputs. Given the phenomenological nature of our
270 neuron model, it is hard to predict how such differences would be reflected, given the diverse dynamical
271 properties that can arise from the dendritic structure (Häusser et al., 2000). The two models tested in
272 our study can be regarded as two extreme cases, where the point neuron represents a completely linear
273 superposition of inputs and the compartment model being strongly nonlinear with respect to proximal
274 and distal inputs. In principle, pyramidal structures could also exhibit properties in between, where the
275 resulting plasticity processes would show a mixture between the classical point neuron behavior (e.g. if a
276 dimensionality reduction of the input via PCA is the main task) and a regime dominated by proximal-distal
277 input correlations if top-down signals should be predicted.

278 4.3 Outlook

279 Here we concentrated on one-dimensional distal inputs. For the case of higher-dimensional distal input
280 patterns, as for structured multi-layered networks, it thus remains to be investigated how target signals are
281 formed. However, as previous works have indicated, random top-down weights are generically sufficient for
282 successful credit assignment and learning tasks (Lillicrap et al., 2016; Guergiev et al., 2017). Therefore, we

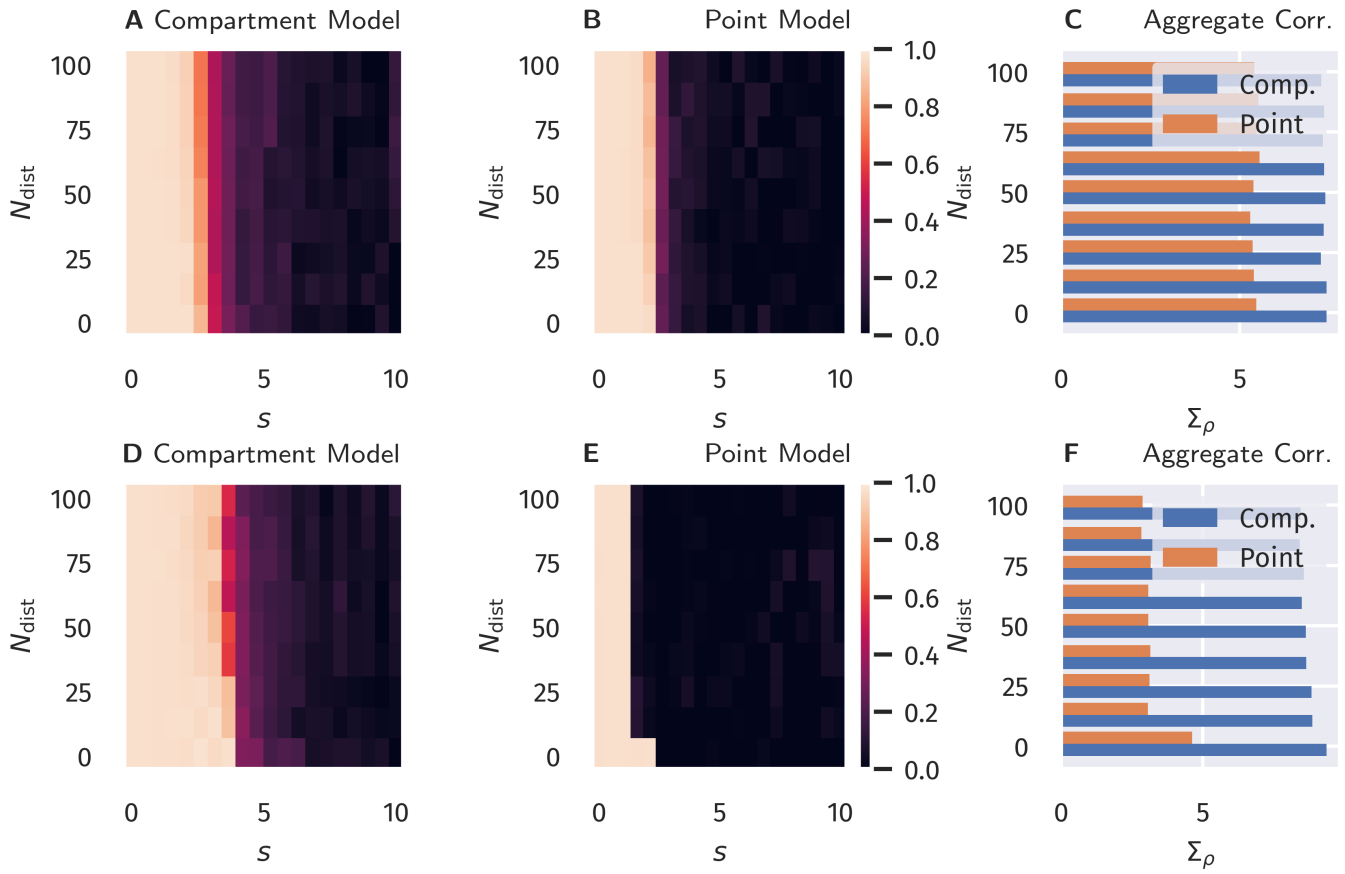


Figure 5. Alignment between Basal and Apical Input after Binary Classification Learning. Correlation between proximal and distal inputs after training, as described in Sect. 3.2. A–C: Classical Hebbian plasticity. D–F: BCM rule. In the bar plot on the right the sum Σ_{acc} over $s = 0, 0.5, 1.0 ..$ of the results is shown as a function of N_{dist} . Blue bars represents the compartment model, orange the point model.

283 expect that our results can be also transferred to deep network structures, for which plasticity is classically
 284 guided by local errors between top-down and bottom-up signals.

5 APPENDIX

285 5.1 Alignment in the Classification Task

286 Instead of measuring the model performance in the classification task presented in Sect. 3.2 by the fraction
 287 of correctly classified patterns, as shown in Fig. 4, one can also use the correlation between I_p and I_d , as
 288 done in Sect. 3.1. This is shown in Fig. 5. One observes a more pronounced difference between the point
 289 model and the compartment model, where the latter results in an overall better alignment for the tested
 290 parameter space.

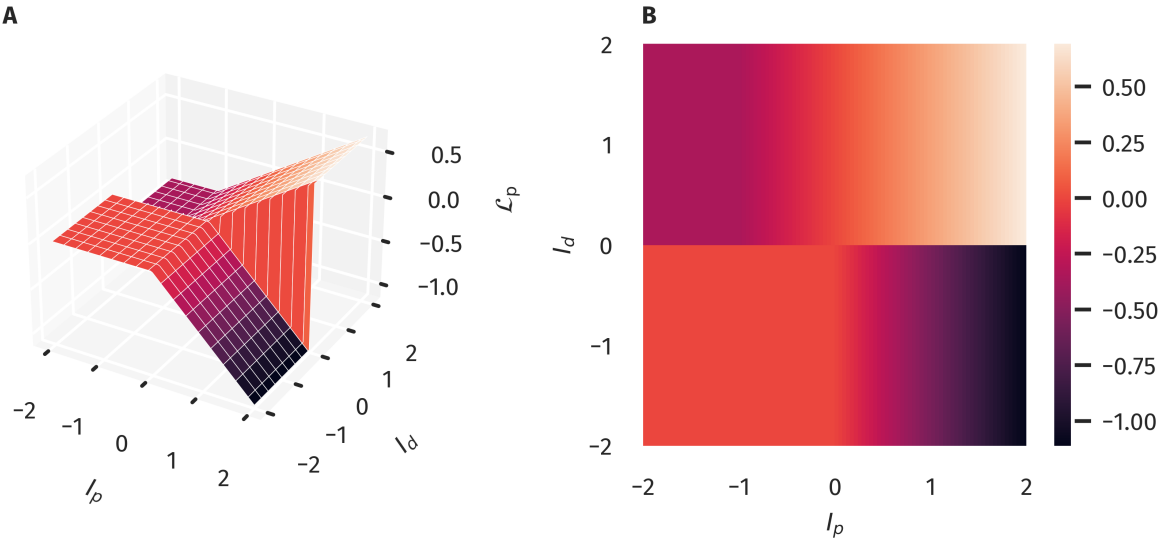


Figure 6. Objective Function for the Proximal Weight Update. The approximate objective function for the proximal weights as given in (22) as a 3d-plot (A) and color-coded (B). This corresponds to a combination of using (1) together with (16). Note the ridge-like structure along the I_p - I_d diagonal, which supports the alignment between proximal and distal input.

291 5.2 Objective Function of BCM Learning in the Compartment Model

292 To gain a better understanding of why the BCM-type learning rule in combination with the implemented
 293 compartment model drives the neuron towards the temporal alignment between I_p and I_d , we can formalize
 294 the learning rule for the proximal weights in terms of an objective function. For this purpose, we further
 295 simplify (1) by replacing the sigmoid functions $\sigma(x)$ by a simple step function $\Theta(x)$. This does not change
 296 the overall shape or topology of the activation in the (I_p, I_d) space but merely makes the smooth transitions
 297 sharp and instantaneous. Using $\Delta w_i \propto y(y - \theta_M)x_i$, we find in this case

$$\Delta w_i \propto \left[(1 - \alpha)\Theta(I_d - \theta_d)\Theta(p - \theta_{p1}) + \alpha(\alpha - 1)\Theta(\theta_d - I_d)\Theta(p - \theta_{p0}) \right] x_i. \quad (21)$$

298 Noting that $\Theta(x)$ is the first derivative of the ReLu function $[x]^+ \equiv \max(0, x)$, we find that this update
 299 rule can be written as

$$\begin{aligned} \Delta w_i &\propto \frac{\partial \mathcal{L}_p}{\partial w_i} \\ \mathcal{L}_p &= (1 - \alpha)\Theta(I_d - \theta_d)[p - \theta_{p1}]^+ + \alpha(\alpha - 1)\Theta(\theta_d - I_d)[p - \theta_{p0}]^+. \end{aligned} \quad (22)$$

300 The objective function \mathcal{L}_p is shown in Fig. 6. One observes that states closer to the I_p - I_d diagonal are
 301 preferred since they tend to yield higher values of \mathcal{L}_p , while the opposite is the case for off-diagonal states.

302 It should be noted, though, that the objective function is not scale-invariant (as would be e.g. if the
 303 squared error was used) in the sense that the prior distributions of both proximal and distal inputs need
 304 a certain mean and variance to cover a region of input states for which the described effects can take
 305 place. As a counterexample, one could imagine that the input samples only covered a flat area of \mathcal{L}_p , as
 306 for example in Fig. 6B in the lower-left quadrant, leading to a zero average gradient. This is prevented,
 307 however, by the homeostatic processes acting simultaneously on the gains and biases, making sure that
 308 the marginal distributions of I_p and I_d are such that higher correlations are preferred. For example, if we

309 assume a Gaussian marginal distribution for both I_p and I_d with zero means and a standard deviation of 0.5
310 (which is used as a homeostatic target in the simulations), the expected value of $\mathcal{L}(I_p, I_d)$ is -0.055 if I_p
311 and I_d are completely uncorrelated, and 0.07 in the perfectly correlated case.

CONFLICT OF INTEREST STATEMENT

312 The authors declare that the research was conducted in the absence of any commercial or financial
313 relationships that could be construed as a potential conflict of interest.

AUTHOR CONTRIBUTIONS

314 Both authors, F.S. and C.G., contributed equally to the writing and review of the manuscript. F.S. provided
315 the code, ran the simulations, and prepared the figures.

ACKNOWLEDGMENTS

316 The authors acknowledge the financial support of the German Research Foundation (DFG)

DATA AVAILABILITY STATEMENT

317 The simulation datasets for this study can be found under <https://cloud.itp.uni-frankfurt.de/s/mSRJ6BPXjwwHmfq>. The simulation and plotting code for this project can be found under
318 https://github.com/FabianSchubert/frontiers_dendritic_coincidence_detection.

REFERENCES

- 320 Bell, A. J. and Sejnowski, T. J. (1995). An Information-maximisation approach to blind separation and
321 blind deconvolution. *Neural Computation* 7, 1129–1159
- 322 Bengio, Y. (2014). How Auto-Encoders Could Provide Credit Assignment in Deep Networks via Target
323 Propagation. *CoRR* abs/1407.7
- 324 Bi, G. Q. and Poo, M. M. (1998). Synaptic modifications in cultured hippocampal neurons: Dependence on
325 spike timing, synaptic strength, and postsynaptic cell type. *Journal of Neuroscience* 18, 10464–10472.
326 doi:10.1523/jneurosci.18-24-10464.1998
- 327 Bienenstock, E. L., Cooper, L. N., and Munro, P. W. (1982). Theory for the development of neuron
328 selectivity: Orientation specificity and binocular interaction in visual cortex. *Journal of Neuroscience* 2,
329 32–48. doi:10.1523/jneurosci.02-01-00032.1982
- 330 Branco, T. and Häusser, M. (2011). Synaptic Integration Gradients in Single Cortical Pyramidal Cell
331 Dendrites. *Neuron* 69, 885–892. doi:10.1016/j.neuron.2011.02.006
- 332 Cannon, J. and Miller, P. (2017). Stable Control of Firing Rate Mean and Variance by Dual Homeostatic
333 Mechanisms. *The Journal of Mathematical Neuroscience* 7, 1
- 334 Clopath, C., Büsing, L., Vasilaki, E., and Gerstner, W. (2010). Connectivity reflects coding: A model of
335 voltage-based STDP with homeostasis. *Nature Neuroscience* 13, 344–352. doi:10.1038/nn.2479
- 336 Debanne, D., Gähwiler, B. H., and Thompson, S. M. (1994). Asynchronous pre- and postsynaptic activity
337 induces associative long-term depression in area CA1 of the rat hippocampus in vitro. *Proceedings of
338 the National Academy of Sciences of the United States of America* 91, 1148–1152. doi:10.1073/pnas.91.
339 3.1148
- 340 Douglas, R. J. and Martin, K. A. (2007). Recurrent neuronal circuits in the neocortex. *Current Biology* 17,
341 R496–R500. doi:10.1016/J.CUB.2007.04.024
- 342 Ebner, C., Clopath, C., Jedlicka, P., and Cuntz, H. (2019). Unifying Long-Term Plasticity Rules for
343 Excitatory Synapses by Modeling Dendrites of Cortical Pyramidal Neurons. *Cell Reports* 29, 4295–
344 4307.e6. doi:10.1016/j.celrep.2019.11.068

- 345 Elston, G. N. (2000). Pyramidal Cells of the Frontal Lobe: All the More Spinous to Think With. *The
346 Journal of Neuroscience* 20
- 347 [Dataset] Elston, G. N. (2003). Cortex, Cognition and the Cell: New Insights into the Pyramidal Neuron
348 and Prefrontal Function. doi:10.1093/cercor/bhg093
- 349 Elston, G. N. and Rosa, M. G. (1997). The occipitoparietal pathway of the macaque monkey: Comparison
350 of pyramidal cell morphology in layer III of functionally related cortical visual areas. *Cerebral Cortex* 7,
351 432–452. doi:10.1093/cercor/7.5.432
- 352 Funahashi, S., Bruce, C. J., and Goldman-Rakic, P. S. (1989). Mnemonic coding of visual space in the
353 monkey's dorsolateral prefrontal cortex. *Journal of Neurophysiology* 61, 331–349. doi:10.1152/jn.1989.
354 61.2.331
- 355 Fuster, J. M. (1973). Unit activity in prefrontal cortex during delayed-response performance: neuronal
356 correlates of transient memory. *Journal of neurophysiology* 36, 61–78. doi:10.1152/jn.1973.36.1.61
- 357 George, D. and Hawkins, J. (2009). Towards a Mathematical Theory of Cortical Micro-circuits. *PLOS
358 Computational Biology* 5, e1000532. doi:10.1371/JOURNAL.PCBI.1000532
- 359 Guergiev, J., Lillicrap, T. P., and Richards, B. A. (2017). Towards deep learning with segregated dendrites.
360 *eLife* 6. doi:10.7554/eLife.22901
- 361 Gustafsson, B., Wigstrom, H., Abraham, W. C., and Huang, Y. Y. (1987). Long-term potentiation in the
362 hippocampus using depolarizing current pulses as the conditioning stimulus to single volley synaptic
363 potentials. *Journal of Neuroscience* 7, 774–780. doi:10.1523/jneurosci.07-03-00774.1987
- 364 Haga, T. and Fukai, T. (2018). Dendritic processing of spontaneous neuronal sequences for single-trial
365 learning. *Scientific Reports* 8, 15166. doi:10.1038/s41598-018-33513-9
- 366 Härdle, W. and Simar, L. (2007). Canonical Correlation Analysis. In *Applied Multivariate Statistical
367 Analysis* (Berlin, Heidelberg: Springer Berlin Heidelberg). 321–330. doi:10.1007/978-3-540-72244-1\\
368 _14
- 369 [Dataset] Häusser, M., Spruston, N., and Stuart, G. J. (2000). Diversity and dynamics of dendritic signaling.
370 doi:10.1126/science.290.5492.739
- 371 Hay, E., Hill, S., Schürmann, F., Markram, H., and Segev, I. (2011). Models of Neocortical Layer
372 5b Pyramidal Cells Capturing a Wide Range of Dendritic and Perisomatic Active Properties. *PLoS
373 Computational Biology* 7, e1002107. doi:10.1371/journal.pcbi.1002107
- 374 Intrator, N. and Cooper, L. N. (1992). Objective function formulation of the BCM theory of visual
375 cortical plasticity: Statistical connections, stability conditions. *Neural Networks* 5, 3–17. doi:10.1016/
376 S0893-6080(05)80003-6
- 377 [Dataset] Larkum, M. (2013). A cellular mechanism for cortical associations: An organizing principle for
378 the cerebral cortex. doi:10.1016/j.tins.2012.11.006
- 379 Larkum, M. E., Kaiser, K. M. M., and Sakmann, B. (1999). Calcium electrogenesis in distal apical dendrites
380 of layer 5 pyramidal cells at a critical frequency of back-propagating action potentials. *Proceedings of
381 the National Academy of Sciences* 96, 14600–14604. doi:10.1073/PNAS.96.25.14600
- 382 Larkum, M. E., Nevian, T., Sandier, M., Polsky, A., and Schiller, J. (2009). Synaptic integration
383 in tuft dendrites of layer 5 pyramidal neurons: A new unifying principle. *Science* 325, 756–760.
384 doi:10.1126/science.1171958
- 385 Law, C. C. and Cooper, L. N. (1994). Formation of receptive fields in realistic visual environments
386 according to the Bienenstock, Cooper, and Munro (BCM) theory. *Proceedings of the National Academy
387 of Sciences of the United States of America* 91, 7797–7801. doi:10.1073/pnas.91.16.7797
- 388 Lee, D. H., Zhang, S., Fischer, A., and Bengio, Y. (2015). Difference target propagation. In *Lecture Notes
389 in Computer Science (including subseries Lecture Notes in Artificial Intelligence and Lecture Notes in*

- 390 *Bioinformatics*) (Springer Verlag), vol. 9284, 498–515. doi:10.1007/978-3-319-23528-8_31
- 391 Letzkus, J. J., Kampa, B. M., and Stuart, G. J. (2006). Learning Rules for Spike Timing-Dependent
392 Plasticity Depend on Dendritic Synapse Location. *Journal of Neuroscience* 26, 10420–10429. doi:10.
393 1523/JNEUROSCI.2650-06.2006
- 394 Lillicrap, T. P., Cownden, D., Tweed, D. B., and Akerman, C. J. (2016). Random synaptic feedback
395 weights support error backpropagation for deep learning. *Nature Communications* 7, 1–10. doi:10.1038/
396 ncomms13276
- 397 Linsker, R. (1986). From basic network principles to neural architecture: emergence of orientation-
398 selective cells. *Proceedings of the National Academy of Sciences of the United States of America* 83,
399 8390. doi:10.1073/PNAS.83.21.8390
- 400 Luebke, J. I. (2017). Pyramidal Neurons Are Not Generalizable Building Blocks of Cortical Networks.
401 *Frontiers in Neuroanatomy* 11, 11. doi:10.3389/FNANA.2017.00011
- 402 Markram, H., Lübke, J., Frotscher, M., and Sakmann, B. (1997). Regulation of synaptic efficacy by
403 coincidence of postsynaptic APs and EPSPs. *Science* 275, 213–215. doi:10.1126/science.275.5297.213
- 404 Park, J., Papoutsi, A., Ash, R. T., Marin, M. A., Poirazi, P., and Smirnakis, S. M. (2019). Contribution
405 of apical and basal dendrites to orientation encoding in mouse V1 L2/3 pyramidal neurons. *Nature
406 Communications* 2019 10:1 10, 1–11. doi:10.1038/s41467-019-13029-0
- 407 Poirazi, P. (2009). Information processing in single cells and small networks: Insights from compartmental
408 models. In *AIP Conference Proceedings* (American Institute of Physics), vol. 1108, 158–167. doi:10.
409 1063/1.3117124
- 410 [Dataset] Ramaswamy, S. and Markram, H. (2015). Anatomy and physiology of the thick-tufted layer 5
411 pyramidal neuron. doi:10.3389/fncel.2015.00233
- 412 Schiess, M., Urbanczik, R., and Senn, W. (2016). Somato-dendritic Synaptic Plasticity and Error-
413 backpropagation in Active Dendrites. *PLoS Computational Biology* 12, 1004638. doi:10.1371/journal.
414 pcbi.1004638
- 415 Schubert, F. and Gros, C. (2021). Local Homeostatic Regulation of the Spectral Radius of Echo-State
416 Networks. *Frontiers in Computational Neuroscience* 15, 12. doi:10.3389/FNCOM.2021.587721
- 417 Shai, A. S., Anastassiou, C. A., Larkum, M. E., and Koch, C. (2015). Physiology of Layer 5
418 Pyramidal Neurons in Mouse Primary Visual Cortex: Coincidence Detection through Bursting. *PLOS
419 Computational Biology* 11
- 420 Sjöström, P. J. and Häusser, M. (2006). A Cooperative Switch Determines the Sign of Synaptic Plasticity
421 in Distal Dendrites of Neocortical Pyramidal Neurons. *Neuron* 51, 227–238. doi:10.1016/j.neuron.2006.
422 06.017
- 423 Spruston, N. (2008). Pyramidal neurons: dendritic structure and synaptic integration. *Nature Reviews
424 Neuroscience* 9, 206–221. doi:10.1038/nrn2286
- 425 Spruston, N., Schiller, Y., Stuart, G., and Sakmann, B. (1995). Activity-dependent action potential invasion
426 and calcium influx into hippocampal CA1 dendrites. *Science* 268, 297–300. doi:10.1126/science.
427 7716524
- 428 Stuart, G. J. and Häusser, M. (2001). Dendritic coincidence detection of EPSPs and action potentials.
429 *Nature Neuroscience* 4, 63–71. doi:10.1038/82910
- 430 Triesch, J. (2007). Synergies Between Intrinsic and Synaptic Plasticity Mechanisms. *Neural Computation*
431 19, 885–909. doi:10.1162/neco.2007.19.4.885
- 432 Urbanczik, R. and Senn, W. (2014). Learning by the Dendritic Prediction of Somatic Spiking. *Neuron* 81,
433 521–528. doi:10.1016/j.neuron.2013.11.030

- 434 Weissenberger, F., Gauy, M. M., Lengler, J., Meier, F., and Steger, A. (2018). Voltage dependence of
435 synaptic plasticity is essential for rate based learning with short stimuli. *Scientific Reports* 8, 4609.
436 doi:10.1038/s41598-018-22781-0
- 437 Yger, P. and Gilson, M. (2015). Models of Metaplasticity: A Review of Concepts. *Frontiers in*
438 *Computational Neuroscience* 9, 138. doi:10.3389/FNCOM.2015.00138